



Valence-change bipolar resistive switching devices based on ErMnO₃ polymorphs



Rong Wu , Florian Maudet¹, Thanh Luan Phan¹, Sebastian W. Schmitt¹, Veeresh Deshpande¹ & Catherine Dubourdieu

Memristive devices, which emulate the synaptic behavior of biological systems, are at the forefront of next-generation memory and neuromorphic computing technologies. Here, we investigate bipolar resistive switching in Pt/polycrystalline ErMnO₃/Ti/Au memristive devices and show how mixed orthorhombic and hexagonal ErMnO₃ polymorph films can be engineered to optimize the device performance. The two crystalline phases are evidenced by a combination of correlative microscopies (scanning electron microscopy, optical microscopy and conductive atomic force microscopy) and Raman spectroscopy. The devices exhibit high $R_{\text{OFF}}/R_{\text{ON}}$ ratios ($\sim 10^5$) and ultra-low R_{ON} resistances ($\sim 10 \Omega$). The resistive switching is the result from the formation and rupture of an oxygen-vacancy-based conductive filament, which likely occurs either in the orthorhombic phase or at the boundary between the two polymorphs. An increased fraction of orthorhombic phase strongly reduces the operating voltage (down to $V_{\text{Set}} \sim -2.07 \text{ V}$) and its variability. The presence of the hexagonal phase, which is much less conductive than the orthorhombic one, reduces leakage currents in the devices, that otherwise would not exhibit switching behavior.

Hexagonal rare-earth manganites h-RMnO₃ (R = Y, Er, Ho to Lu) have attracted great attention due to their remarkable multiferroic properties. These materials exhibit a “cloverleaf”-like ferroelectric domain structure^{1–3}, as well as charged and neutral functional domain walls^{4–9}. Among the multiferroelectric compounds, ErMnO₃ stands out as one of the most intensively researched systems. However, the majority of studies to date have focused primarily on single crystals^{5,10,11}, lamellae⁷, or ceramics¹², which limits their integrability into devices.

Recently, studies have shown demonstrations of non-volatile resistive switching behavior in both stoichiometric and off-stoichiometric polycrystalline hexagonal YMnO₃ thin films, generating interest for potential neuromorphic applications^{13–18}. While many binary and ternary oxides also exhibit resistive switching behavior, the study of h-RMnO₃ holds promise to eventually combine ferroelectricity and resistive switching to offer an additional knob for designing multilevel analog devices. Moreover, we recently showed that using a mixture of the hexagonal and orthorhombic polymorph phases in YMnO₃ films brings new functionalities via the boundaries between nanograins of both phases¹⁹.

For ErMnO₃, the hexagonal phase is the thermodynamically stable phase at room temperature and atmospheric pressure. However, like for YMnO₃, there is only a small difference in free energy (<5 kJ/mol) with the

metastable orthorhombic phase^{20,21}. This leads to the occurrence of the orthorhombic phase when processing conditions are favorable. Previous works have shown that orthorhombic form of hexagonal manganites (RMnO₃, R = Y-Lu) can be obtained at high pressure^{22–27}, or by epitaxial phase stabilization^{28–32}. Hence, mixed crystalline phases can coexist in polycrystalline thin films due to substrate-induced stress^{19,26,33}. The orthorhombic phase of YMnO₃ has a higher electrical conductivity than the hexagonal one^{19,34}, indicating that a similar trend could be expected for ErMnO₃. To the best of our knowledge, there has been so far no report on resistive switching in devices based on ErMnO₃ films.

In this study, we investigate the impact of mixed hexagonal and orthorhombic ErMnO₃ (h-ErMnO₃, o-ErMnO₃) phases and of their relative content on the resistive switching of Pt/ErMnO₃/Ti/Au memristive devices. Using correlative microscopies and Raman spectroscopy we identify the presence of o-ErMnO₃ and quantify the relative amounts of o- and h-ErMnO₃ phases. The devices demonstrate a bipolar resistive switching behavior based on valence change mechanism with the formation and rupture of an oxygen-vacancy-based conductive filament. The increase of the orthorhombic phase content allows for reducing the OFF-state resistance, R_{OFF} , as well as the Set voltage, V_{Set} , and its variability. The devices with more than 60% orthorhombic phase do not exhibit resistive switching behavior.

¹Helmholtz-Zentrum Berlin für Materialien und Energie, Berlin, Germany. ²Freie Universität Berlin, Physical and Theoretical Chemistry, Berlin, Germany.

e-mail: rong.wu@helmholtz-berlin.de; catherine.dubourdieu@helmholtz-berlin.de

Results and discussion

Microstructural characterization of ErMnO₃

Figure 1a illustrates the device fabrication process and film characterization steps for metal-ErMnO₃-metal devices. The details are provided in the “Method” section. An optical microscopy image of a fabricated device is shown in Supplementary Fig. S1.

The grazing incident X-ray diffraction patterns of an as-deposited and subsequently annealed stack are shown in Fig. 2a. The as-deposited ErMnO₃ film is amorphous (all XRD peaks match the bottom Pt electrode)³⁵. After annealing, most peaks correspond to the hexagonal structure (*P63cm* space group) of ErMnO₃²⁵. The other minor peaks correspond to the orthorhombic structure (*Pnma* space group) of ErMnO₃³⁶.

As discussed in the introduction, previous studies have shown that the orthorhombic phase can be stabilized under high pressure using bulk synthesis techniques^{22–27} or by epitaxial strain in thin films^{28–32}. The occurrence of the orthorhombic phase in our films is associated with the substrate-induced strain imparted by the Pt substrate upon cooling from high temperature (750 °C) to room temperature. This observation is consistent with findings in polycrystalline YMnO₃, which exhibits a mixture of hexagonal and orthorhombic phases on Pt-coated Si substrates¹⁹. The high-pressure effect associated with strain also results in a reduction of the lattice parameters *a* and *c* of the hexagonal phase (Table 1), much lower than those

of polycrystalline bulk formed under atmospheric pressure²⁵ but similar to those of polycrystalline bulk prepared at 6.7 GPa²⁶. More quantitative strain analysis could be investigated in the future using electron backscatter diffraction for grain orientation and strain distribution, along with transmission electron microscopy with geometric phase analysis for high-resolution strain mapping.

Grazing incident X-ray diffraction does not allow for an accurate quantification of the fraction of both crystalline phases, as many peaks cannot be unambiguously assigned to one or the other phase. Some of them indeed overlap. Moreover, the films are nanocrystalline (with grain size of the order of ~ 50 nm) and therefore some peaks might be too weak to be recorded. We developed a method combining microscopies and Raman spectroscopy to quantitatively determine the amount of each crystalline phase, which has been previously applied to YMnO₃ thin films¹⁹. Optical microscopy and SEM images of annealed ErMnO₃ are shown in Fig. 2b, c, respectively. Both types of images exhibit bright and dark contrasts, with similar features at the same spots. Composition and topography are the two dominant factors that are responsible for the contrast in SEM. Meier et al. reported an SEM investigation of ErMnO₃ single crystals and associated bright and dark areas to upward and downward ferroelectric domain polarizations, respectively^{37,38}. Therefore, to disambiguate between the different possibilities of the origin of the contrast, we performed Raman

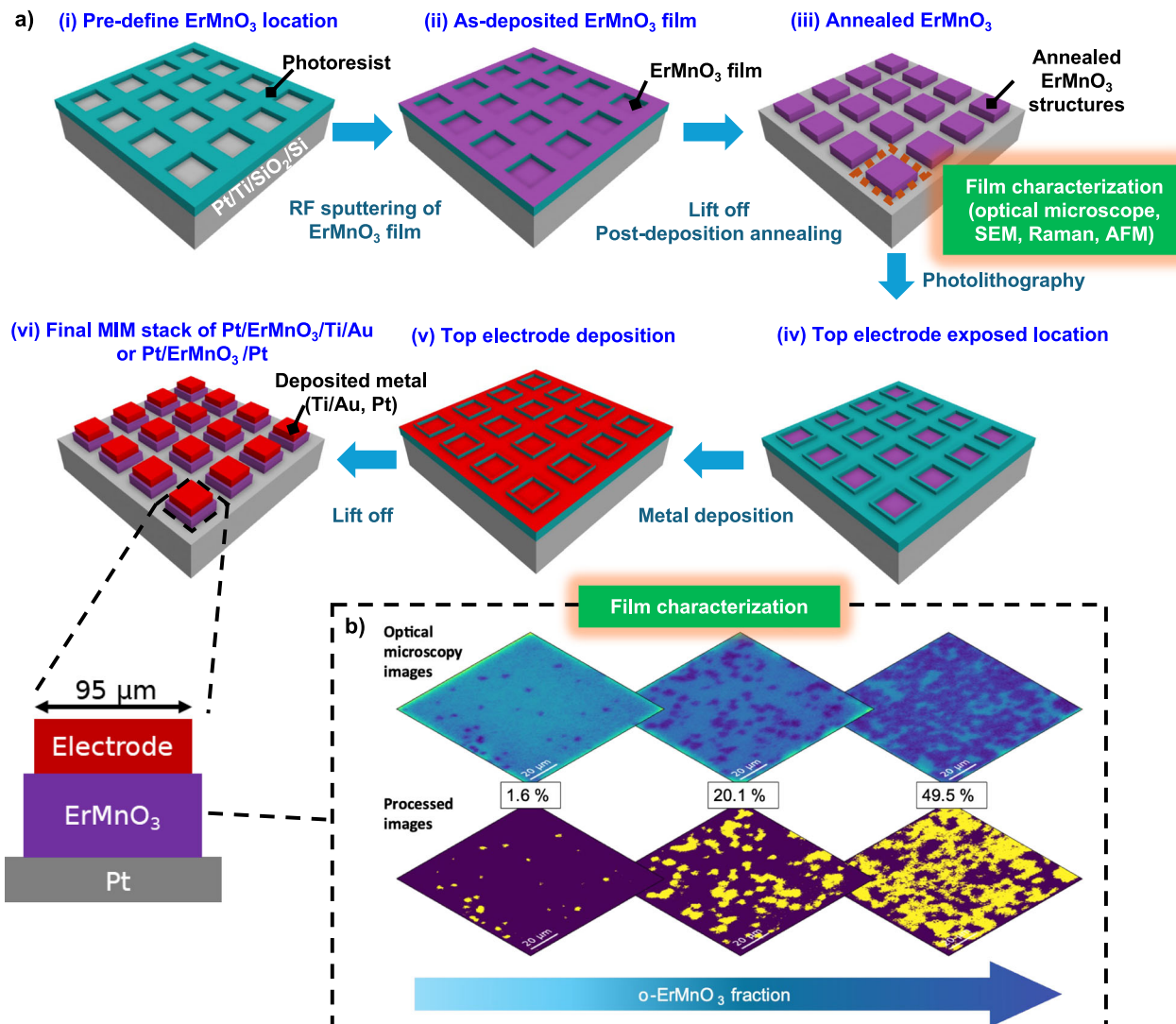


Fig. 1 | Schematics of the device fabrication process and film characterization. a Fabrication process flow. The top electrodes have a size of 95 × 95 μm². The details are provided in the Method section. b Optical microscopy images with different

fractions of bright blue/dark blue contrast regions and segmentation results for the estimation of the fraction of dark-contrast region area (o-ErMnO₃) relatively to the bright one (h-ErMnO₃).

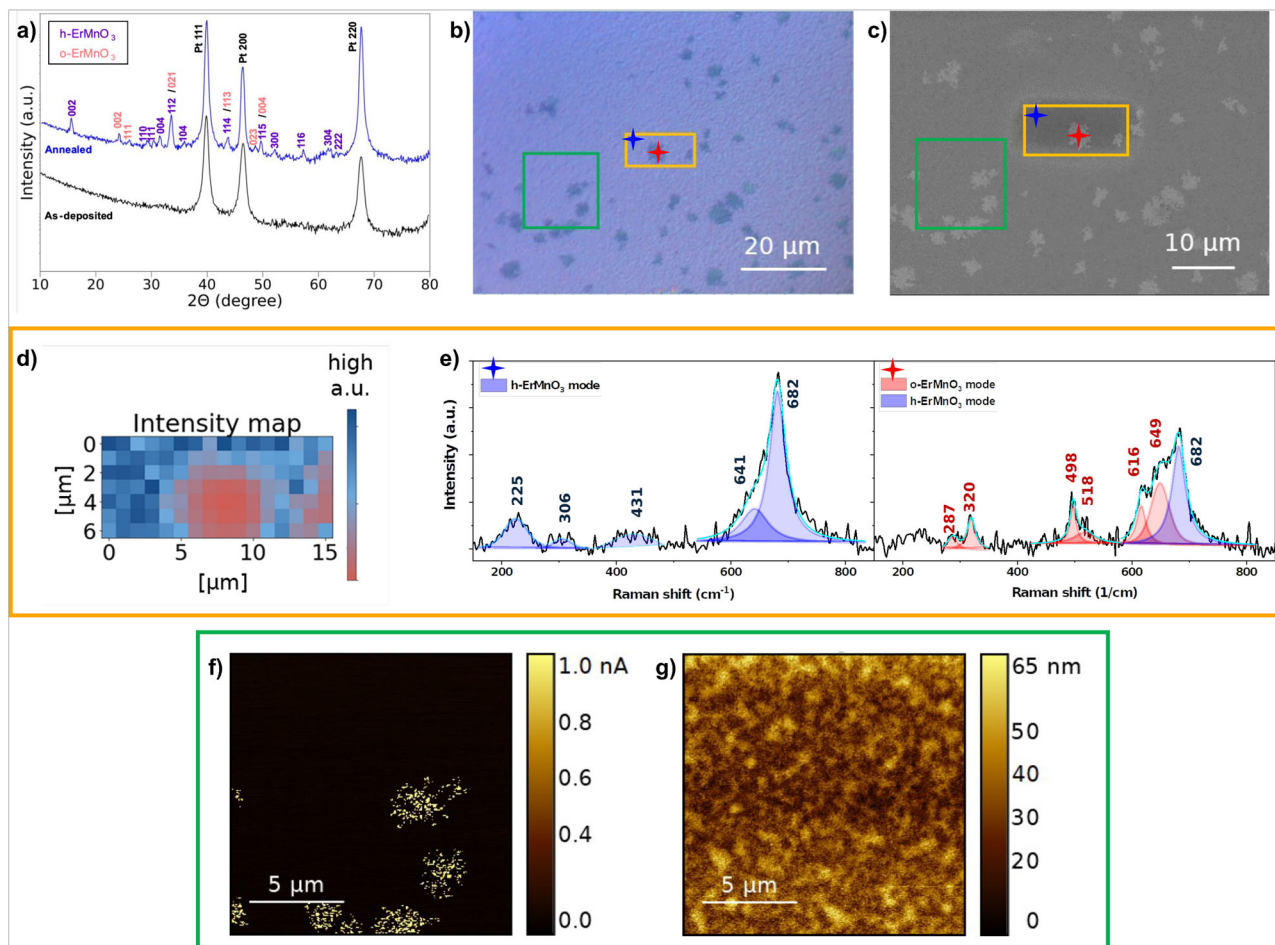


Fig. 2 | Structural characterization of ErMnO₃. **a** Grazing incidence X-ray diffraction of an as-deposited and annealed square-patterned ErMnO₃ on Si/SiO₂/Ti/Pt substrate. **b** Optical microscopy image and **c** SEM image of an annealed ErMnO₃ structure. **d** Raman intensity map of the region marked by the yellow box shown in **(b)** and **(c)** based on the mode A₁(TO₉) at 682 cm⁻¹ from h-ErMnO₃ phase. **e** Two

Raman spectra with their fitted Raman modes recorded at the positions marked with red and blue stars are indicated in **(b, c)**. **f** Current map obtained by conductive-AFM and **g** corresponding topographic map collected in the area marked by the green rectangle shown in **(b)** and **c** on an annealed ErMnO₃ structure.

Table 1 | Lattice parameters and unit cell volume of hexagonal phase in the ErMnO₃ structures, and of polycrystalline bulk formed under 0 GPa²⁵ and 6.7 GPa²⁶

Sample	In plane lattice <i>a</i> (Å)	Out of plane lattice <i>c</i> (Å)	Volume of cell (Å ³)
Polycrystalline bulk (0 GPa) ²⁵	6.12	11.41	370.28
Polycrystalline bulk (6.7 GPa) ²⁶	6.03*	11.35*	358.17*
Polycrystalline thin film (this work)	6.03	11.34	357.88

The 111 peak at $2\theta = 40.0^\circ$ of Pt was taken as a reference. The in-plane *a* and out-of-plane *c* lattice parameters were calculated from the highest intensity peaks, 110 and 004, respectively.
*The values were derived by extracting data from Fig. 2 in ref. 26.

spectroscopy on the area indicated by the yellow box in Fig. 2b, c. Raman spectroscopy mapping was performed with the intensity of the A₁(TO₉) mode at 682 cm⁻¹ (scan size of $6 \times 15 \mu\text{m}^2$, beam size of 1 μm and spatial resolution of ~1 μm). This mode corresponds to the apical oxygen atoms (O₁ and O₂) stretching along the *c*-axis in hexagonal ErMnO₃ and is associated with the tilting and trimerization of MnO₅ polyhedra^{39,40}. This mode is absent in the orthorhombic phase. The Raman intensity map shown in Fig. 2d displays two distinct regions colored in blue and red, based on the intensity of the peak at 682 cm⁻¹. Figure 2e presents two Raman spectra performed in these two regions (marked with red and blue stars). The spectra were indexed with the corresponding Raman modes, and the spectral positions are compared to those of single crystals in Table 2. The spectrum obtained from the spot marked with a blue star indicates the

presence of pure hexagonal phase, while the one from the region marked with a red star shows the presence of orthorhombic phase with a minor contribution from the hexagonal phase.

Comparing the Raman intensity map with the optical microscopy and SEM images indicates that low brightness (dark contrast) in optical microscopy and high electron yield in SEM (bright contrast) are signatures of the o-ErMnO₃ crystalline phase. Vice versa, high brightness (bright contrast) in optical microscopy and low electron yield (dark contrast) are signatures of the h-ErMnO₃ crystalline phase. The bright regions (o-ErMnO₃) observed in SEM exhibit irregular and discontinuous shapes. Hence, some measured spots might include small amounts of the surrounding hexagonal phase, which explains the detected mode A₁(TO₉) in the Raman spectrum at the position of the red star in Fig. 2e.

Table 2 | Raman active modes of references (single crystals) and experimental data

Single crystal h-ErMnO ₃ ³⁹ (cm ⁻¹)	Single crystal o-ErMnO ₃ ⁶⁸ (cm ⁻¹)	Spectrum in blue [This work] (cm ⁻¹)	Spectrum in red [This work] (cm ⁻¹)
E ₂ (5) 218	B _{1g} 280	E ₂ (5) 225	B _{1g} 287
E ₂ (8) 295	A _g 316	E ₂ (8) 306	A _g 320
E ₂ (11) 417	A _g 490	E ₂ (11) 431	A _g 498
E ₁ (TO ₁₄) 639	A _g 520	E ₁ (TO ₁₄) 642	A _g 518
A ₁ (TO ₉) 683	B _{1g} 610	A ₁ (TO ₉) 682	B _{1g} 616
	653 ^a		649 ^a
			A ₁ (TO ₉) 682

^aRaman shift is not related to a proper vibration mode from o-ErMnO₃⁶⁹, it might be from defects⁷⁰ or contributions from zone-boundary phonons⁵⁹.

The presence of the orthorhombic phase in the polycrystalline films is further confirmed by conductive atomic force microscopy (c-AFM) measurements. As established in previous studies, h-ErMnO₃^{5,41} and o-ErMnO₃⁴² are p-type semiconductor materials. They are characterized by hopping conduction between Mn³⁺ and Mn⁴⁺ ions^{41,42}. A c-AFM spatial mapping was performed on the area indicated by the green box in Fig. 2b, c. During the measurement, the platinum-coated tip was grounded and a DC bias of 1.5 V was applied to the bottom electrode. The current image is presented in Fig. 2f. The highly conducting regions correlate directly to the dark and bright regions in the optical microscopy and SEM images, respectively (Fig. 2b, c), identified as o-ErMnO₃ by Raman spectroscopy (Fig. 2d). The c-AFM results confirm the high and low conductivity of o-ErMnO₃ and h-ErMnO₃, respectively. The topographic image shown in Fig. 2g reveals no significant surface morphology difference between the different conductive regions. We can therefore exclude a topographic contribution to the observed bright/dark contrasts in the optical microscopy and SEM images.

Through correlative microscopy and spectroscopy analyses, we have clearly identified the presence of the orthorhombic phase in polycrystalline hexagonal EMnO₃ films. Optical microscopy offers a rapid and straightforward method to assess the coexistence of both phases and enables a quantitative analysis. We assume that the orthorhombic phase regions extend down to the bottom interface (Pt substrate) since we can detect them by c-AFM.

Optical microscopy images were captured on individual ErMnO₃ structures ($100 \times 100 \mu\text{m}^2$). Representative images with different fractions of dark/bright regions are presented in Fig. 1b (top panel), which were then processed with signal processing algorithms to separate the bright and dark areas representing orthorhombic and hexagonal phases, respectively. With this method, we estimated the fraction of the two crystalline phases in the selected areas. The results of the segmentation treatment of the optical microscopy images are displayed in Fig. 1b (bottom panel), with o-ErMnO₃ fractions varying from ~ 2 to $\sim 50\%$.

Electrical characterization of Pt/ErMnO₃/Ti/Au with minor o-ErMnO₃ content

Current–voltage (I–V) measurements were performed at room temperature on Pt/ErMnO₃/Ti/Au devices with a majority of h-ErMnO₃ (2% o-ErMnO₃, Fig. 3a). A series resistor of 1 kΩ was used to prevent current overshoots leading to irreversible hard breakdown of the device. This passive current limitation can be more effective than active compliance current for these low R_{ON} devices, as it provides instantaneous current control without feedback delay⁴³. The Pt bottom electrode was grounded, and a DC bias was applied to the top electrodes. A negative voltage sweep (from 0 to -15 V back to 0) with a sweep rate of 75 mV/s was applied to the top electrode to switch the device (Set) from pristine high resistance state (HRS, OFF state) to low resistance state (LRS, ON state). Subsequently, the resistance in LRS was determined by Kelvin (4-wire) resistance measurements, which allowed to

calibrate the cable and contact parasitic resistance⁴⁴. A positive voltage sweep (from 0 to 1.3 V back to 0) with a sweep rate of 15 mV/s was then applied to the top electrode to switch the device from LRS back to HRS (Reset). A slower sweep rate was applied to enhance the dissolution of filaments during the Reset process, which will be discussed later. Figure 3b shows I–V curves for 100 cycles (in Fig. 3c the contribution of the 1 kΩ resistor in series has been subtracted to show the voltage V_{Device} across the device). A bipolar resistive switching behavior is observed with Set occurring at negative voltages and Reset occurring at positive voltages. For the initial cycle, a voltage exceeding -10 V is necessary to switch the device from pristine HRS to LRS, indicating the need for a Forming step to initiate the filament.

The log-log scale of the I–V curves in LRS (for $V_{\text{Device}} < 0$), as presented in Fig. 3d, shows a current versus voltage slope approximately equal to 1, indicative of ohmic conduction. The ON resistances of the devices are independent on the electrode area, as shown in Fig. 3e, suggesting a localized filamentary rather than an interfacial or bulk conduction mechanism⁴⁵. The formation of a metallic filament during the Forming and Set processes supports the ohmic conduction in LRS^{46,47}. A stepped decrease of the current is observed during the Reset process, from LRS to HRS (Fig. 3f), which indicates a progressive dissolution of the filament likely occurring by the progressive decrease of its diameter.

Since the Forming and Set processes occur under a negative electric field, the filament formation is mostly driven by a valence change mechanism involving oxygen vacancies. Waser et al. proposed that redox-based memristive cells typically consist of two metal electrodes with different work functions, creating a Schottky and an ohmic-like contact^{48,49}. This electrode asymmetry is essential for resistive switching, as it enables directional control of filament formation and rupture, depending on applied bias^{48–50}. In our case, ErMnO₃, a p-type semiconductor, forms a Schottky contact with the low work function metal Ti and an ohmic contact with the high work function metal Pt. When a negative voltage is applied to the top electrode, positively charged oxygen vacancies move toward the Schottky interface, forming a conductive channel in the ErMnO₃ layer, leading to the switching from HRS to LRS. The switching takes place near the interface of the Schottky contact^{48,49} and the filament extends from top to bottom across the film. When a positive voltage is applied, the filament ruptures due to electrochemical re-oxidation (the oxygen vacancies are moving away from the top electrode) and Joule heating, causing the device to switch back from LRS to HRS.

The distribution of Set and Reset voltages over the 100 cycles (Fig. 3g) shows a relatively large variability in V_{Set} (-2.3 ± 0.5 V) and a low variability in V_{Reset} (0.35 ± 0.07 V). Figure 3h presents the distribution of R_{OFF} and R_{ON} over the 100 sweeps. A high $R_{\text{OFF}}/R_{\text{ON}}$ in the range of 10^4 – 10^5 and an ultra-low ON resistance (10.3 ± 1.7 Ω) are achieved. Figure 3i presents the retention measurement of a device, showing no drift in HRS and LRS states over 6×10^3 s.

Prior studies have reported that defects, such as oxygen vacancies, can be induced in various oxide switching layers due to the oxygen-gettering activity of the Ti electrode^{51–53}. In our case, the primary role of the Ti electrode is not to generate oxygen vacancies; the oxygen vacancies are intrinsic to the material consisting of the polymorph mixtures. This is evidenced when considering Pt/ErMnO₃/Pt stacks where the top electrode has been replaced by Pt. These stacks were characterized and compared to the Pt/ErMnO₃/Ti/Au ones (Supplementary Fig. S2). For both cases, devices containing 2% o-ErMnO₃ were selected. In general, the resistances in pristine state of Ti top electrode devices were found to be larger than those with Pt top electrodes (Supplementary Fig. S2b, c). This can be attributed to the higher Ti/ErMnO₃ Schottky barrier height compared to the Pt/ErMnO₃ one (Supplementary Fig. S3). HRS and LRS resistances are quite similar for both stacks (Supplementary Fig. S2c). The distribution of Set and Reset voltages for both stacks is shown in Supplementary Fig. S2d. There is a minimal impact of the top electrode metal on the Forming voltages. The oxygen vacancies needed to form the filament are already present in the ErMnO₃ polycrystalline

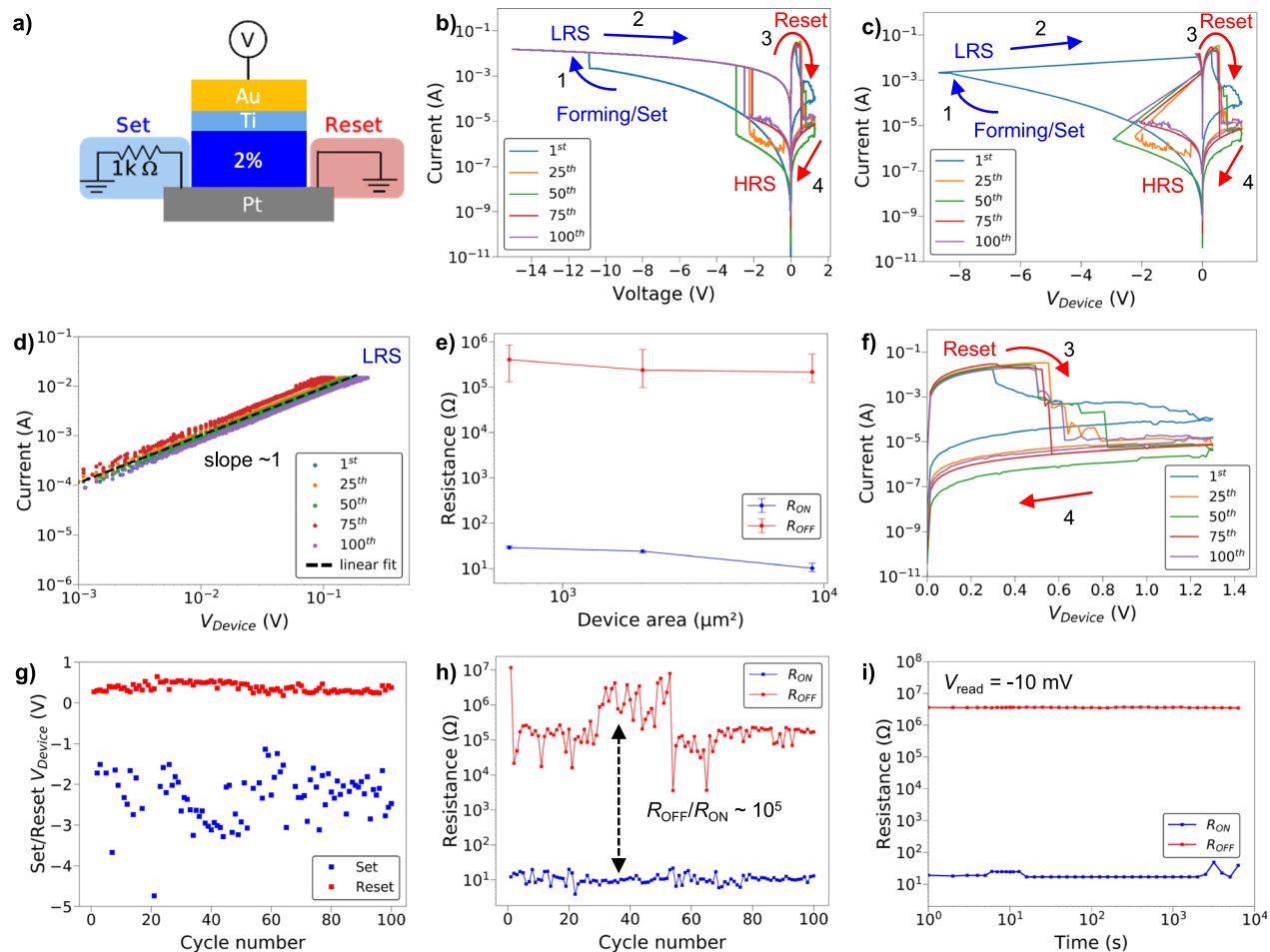


Fig. 3 | *I–V* characteristics of a Pt/ErMnO₃/Ti/Au device with 2% o-ErMnO₃ (98% h-ErMnO₃). **a** Device stack and circuit configuration with a 1 kΩ resistor in series, which avoids current overshoot during Forming and Set processes. **b** Typical *I–V* curves including the contribution of the 1 kΩ resistor in series. **c** *I–V_{Device}* curves where *V_{Device}* is the voltage dropped across the device. **d** Log-log scale *I–V_{Device}* curves in LRS (*V_{Device}* < 0). The absolute values of current and voltage are used in the

log-log plot. The linear fit (black dotted line) with a slope of 1 indicates an ohmic conduction in LRS. **e** Area dependence of the resistances in HRS and LRS. **f** Zoom on the *I–V_{Device}* curves for the Reset process. **g** Variations over 100 cycles of Set and Reset voltage values. **h** Variations over 100 cycles of the *R_{OFF}* and *R_{ON}* values (the OFF resistance was read at -50 mV). Note **g**, **h** are cycle-to-cycle variability test and not meant as endurance test. **i** Retention measurement for the two resistance states.

films. The difference lies in the larger Set voltage values and their larger variability with the Pt top electrode, with a *V_{Set}* of -6.0 V and an interquartile (IQR) of 5.9 V, compared to the Ti top electrode, which has a *V_{Set}* of -2.3 V and an IQR of 3.8 V. Pt/ErMnO₃/Pt stack with symmetric electrode configuration does not have a preferential switching polarity, which increases the variability in operating voltages and limits the switching yield⁵². Ti has a facilitator role in providing additional oxygen vacancies near the top electrode to close the conducting oxygen vacancy filament, leading to a lower *V_{Set}*. Note that the Pt/ErMnO₃/Pt stack devices have very poor endurance (less than 20 cycles), which highlights the role of the top Ti electrode in providing a source of oxygen vacancy exchange.

Impact of the crystalline phase ratio

We investigated three groups of devices with different o-ErMnO₃ fractions: 2% (98% h-ErMnO₃), 20% and 50%. Devices with more than 60% of o-ErMnO₃ did not switch and showed a high level of leakage currents (shown in Supplementary Fig. S4), which indicates that the presence of the hexagonal phase plays a critical role in preventing large leakage currents. The setup for the measurements is shown in Fig. 4a. For devices with 50% o-ErMnO₃, which exhibit significantly larger leakage currents, we employed a 15 mA compliance current during Forming and Set processes instead of the 1 kΩ series resistor (which would have been impractical), as this provides comparable current limitation while accommodating the increased conductivity.

The *I–V* curves for the first sweeps are shown in Fig. 4b (where *V* is the total voltage dropped on the resistor and device) and a zoom on the low negative bias and on the positive bias range is shown in Fig. 4c (where *V_{Device}* is the voltage dropped across the device).

In the LRS, a current versus voltage slope of ~1 (Fig. 4d) indicates an ohmic conduction behavior (*I* ∝ *V*) in all devices with the different o-ErMnO₃ fractions, pointing out to the metallic filament nature of the conduction path.

In the OFF state the leakage currents increase as the o-ErMnO₃ fraction increases, which is due to the larger conductivity of the orthorhombic phase as compared to the hexagonal one (Fig. 2f). To get insight into the conduction mechanisms in the pristine OFF state, we examined two mechanisms commonly observed in this complex oxide, as reported in prior studies^{54–56}. One of these mechanisms is Schottky emission, where thermally activated electrons can cross over the energy barrier and be injected into the conduction band of the semiconductor⁵⁷. In this model, the current dependence on applied voltage is expressed as:

$$\ln\left(\frac{I}{T^2}\right) = \frac{q\sqrt{q/4\pi\epsilon_i d}}{kT} \sqrt{V} - \frac{q\phi_B}{kT} \quad (1)$$

where *I* is the current, *V* is the external applied voltage, ϕ_B is the Schottky barrier height, ϵ_i is the permittivity of the switching layer, *k* is the Boltzmann's constant, *T* is the absolute temperature, and *d* is the Schottky distance.

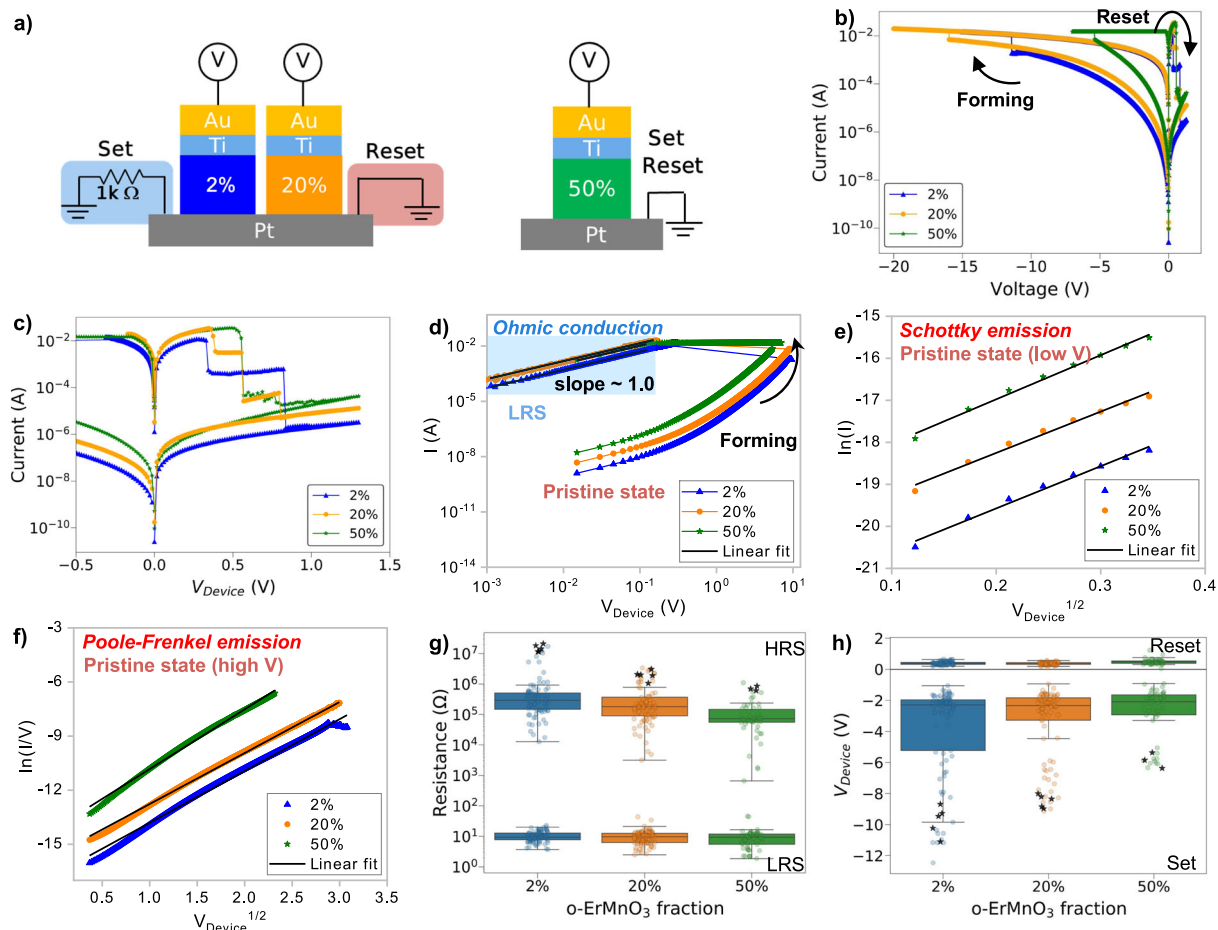


Fig. 4 | Electrical characterization of Pt/ErMnO₃/Ti/Au devices with different fractions of o-ErMnO₃ (2%, 20% and 50%). **a**, Device architecture and its operational configuration during Forming, Set and Reset measurements. A 1 kΩ resistor is connected (to limit the current) during the Set process for devices with 2 and 20% o-ErMnO₃ while a compliance of 15 mA is used for the devices with 50% o-ErMnO₃. **b**, Forming and Reset I - V curves for devices with different fractions of o-ErMnO₃. **c**, Zoom of the I - V_{Device} curves (V_{Device} is the voltage across the device). **d**, Log-log scale I - V_{Device} curves during the Forming process. The linear fits (black lines) indicate an ohmic conduction in LRS for all devices. **e**, $\ln(I)$ - $V_{Device}^{1/2}$ curves in the

low electric field regime ($V_{Device} < 0.7$ V) for the pristine state and their linear fits (black lines), consistent with a Schottky emission model. **f**, $\ln(I/V_{Device})$ - $V_{Device}^{1/2}$ plots at high electric field regime ($V_{Device} > 0.7$ V) for the pristine state, and their linear fits (black lines) consistent with a Poole-Frenkel emission model. **g**, The distribution of the device resistances in the pristine state (star symbols), HRS and LRS (open circles) for different o-ErMnO₃ fractions. **h**, The distribution of Forming voltage (star symbols), Set and Reset (open circles) voltages across the devices for different o-ErMnO₃ fractions. The OFF resistance was read at -50 mV.

We also tested the Poole–Frenkel mechanism, which considers a bulk conduction process where thermally activated electrons are emitted from traps into the conduction band of the semiconductor⁵⁷. In this model, the relation between I and V is given by:

$$\ln\left(\frac{I}{V}\right) = \frac{q\sqrt{q/\pi\epsilon_0 d}}{kT} \sqrt{V} - \frac{q\phi_T}{kT} + \ln(q\mu N_c) \quad (2)$$

where ϕ_T is the trap energy barrier height, di is the dielectric thickness, μ is the mobility of the carriers, and N_c is the density of carriers.

At low voltage regime ($V_{Device} < 0.7$ V), a liner correlation between $\ln(I)$ and $V^{1/2}$ is observed in all devices with varying o-ErMnO₃ fractions, which indicates a Schottky conduction mechanism (Eq. 1, $R^2 = 0.99$), as illustrated in Fig. 4e. The values for the intercept and slope are given in Table 3. The calculated ϕ_B values of three different devices, based on the intercepts ($-\frac{q\phi_B}{kT} + 2\ln(T)$), are also provided in Table 3, for a room temperature $T = 298.15$ K. The decreasing absolute values of the intercept with increasing o-ErMnO₃ fraction suggests a reduction in the Schottky barrier height ϕ_B as the o-ErMnO₃ fraction increases. For 2% o-ErMnO₃ (98% h-ErMnO₃), ϕ_B is of 0.85 eV.

The theoretical barrier height between the metal and pure h-ErMnO₃ can be estimated using the following equation:

$$\phi_B = E_g + \chi - \phi_m \quad (3)$$

where E_g represents the band gap energy of the semiconductor, χ is its electron affinity, and ϕ_m is the metal work function.

Considering for Pt a work function ϕ_m of 5.12 eV⁵⁸, and for h-ErMnO₃ a band energy E_g of 1.6 eV⁵⁹ and an electron affinity χ of 4.6 eV⁵⁹, the theoretical Schottky barrier value is 1.08 eV. The value extracted from the fitting for devices with 98% h-ErMnO₃ (0.85 eV) is lower, which is coherent with the fact that the band gap energy of orthorhombic RMnO₃ is smaller than that of the hexagonal phase⁶⁰.

The experimentally calculated ϕ_B values decrease as the orthorhombic phase fraction increases, which aligns with the earlier argument. The Schottky slope values, derived from $\frac{q\sqrt{q/4\pi\epsilon_0 d}}{kT}$, remain independent of the o-ErMnO₃ fraction, suggesting that the Schottky emission distance d remains constant regardless of the relative o-ErMnO₃ amount.

At a higher voltage regime ($V_{Device} > 0.7$ V), the I - V curves of the pristine state in all devices closely adhere to the Poole-Frenkel emission

Table 3 | Conduction mechanism parameters obtained in the pristine state

Conduction	2% o-ErMnO ₃	20% o-ErMnO ₃	50% o-ErMnO ₃
Schottky intercept	-21.58	-20.22	-19.08
Schottky slope	10.5	9.8	10.1
Schottky barrier	0.85 eV	0.81 eV	0.78 eV
PF intercept	-16.68	-15.59	-14.13
PF slope	3.3	2.8	2.8

model (Eq. 2, $R^2 = 0.99$), as shown in Fig. 4f. The corresponding extracted intercepts and slopes are presented in Table 3. The absolute values of the intercept decrease with increasing o-ErMnO₃ content. The numerical intercept values are derived from the expression $-\frac{q\phi_T}{kT} + \ln(q\mu N_c)$, where the trap energy barrier ϕ_T in h-ErMnO₃ and o-ErMnO₃ are expected to be similar, given that the mobile carrier source comes from Mn⁴⁺ associated holes in the valence band for both polymorphs^{41,42,61}. However, due to a higher concentration of Mn⁴⁺ in o-ErMnO₃ compared to h-ErMnO₃^{34,62}, there is a higher carrier density N_c , resulting in smaller absolute intercept values as the o-ErMnO₃ fraction increases. Regarding the Poole–Frenkel (PF) slope values, determined from $\frac{q\sqrt{q/\pi e di}}{kT}$, they remain similar with the increase of o-ErMnO₃ fraction. This observation implies that the dielectric film thickness remains uniform across all devices, supporting that the o-ErMnO₃ phase extends from the bottom electrode to the film surface.

To summarize, an ohmic conduction is observed in the LRS, while, in the pristine HRS, Schottky emission at low electric field and Poole–Frenkel emission at high electric field are predominant. In subsequent HRS, interface-dominated Schottky emission governs the conduction behavior (see Supplementary Fig. S5). The partial-only dissolution of the filament during Reset (as observed on the I – V curves) weakens the contribution of Poole–Frenkel conduction.

Now, let us discuss the change in device characteristics with the increasing content in o-ErMnO₃. Figures 4g, h presents the distributions of the resistances (HRS and LRS) and of operating voltages (V_{Set} and V_{Reset}), respectively. All data are summarized in the Supplementary Table 1. For each group of orthorhombic phase fractions, we typically analyzed five devices (three for the devices with 50% o-ErMnO₃). The data for the different devices are shown in the Supplementary Fig. S6.

The resistance R_{OFF} in HRS (including in the pristine state) decreases as the o-ErMnO₃ fraction increases, resulting in a slightly smaller memory window since R_{ON} stays constant ($R_{\text{OFF}}/R_{\text{ON}}$ ratio of $\sim 10^4$ for 50% o-ErMnO₃). The incomplete dissolution of the filament during the Reset process leads to resistances in HRS lower than their initial pristine values and to a large R_{OFF} variability, from cycle-to-cycle (Fig. 3h), across devices (Supplementary Fig. S6a), and for all o-ErMnO₃ contents (Fig. 4g). As expected, the mechanism at the origin of the filament rupture (localized Joule heating and redox reaction of oxygen vacancies at the weakest point) does not depend on the content of o-ErMnO₃, thus leading to a relatively constant V_{Reset} distribution and a relatively low cycle-to-cycle, and device-to-device variability for all o-phase contents.

The ON state current (Fig. 4c - below compliance) and R_{ON} values (Fig. 4g) do not depend much on the amount of o-ErMnO₃ phase, which is coherent with a filamentary mechanism. Indeed, the resistance of the filament formed in the o-ErMnO₃ is not expected to change with the proportion of this phase. Hence, the LRS resistance remains relatively constant, around 10 Ω , for all cycles, all devices and all o-phase contents. The large cycle-to-cycle (Fig. 3g) and device-to-device (Fig. 4h and Supplementary Fig. S6b) variability of the Set voltages for each o-ErMnO₃ content originates from the stochastic nature of the filament formation combined with morphological effects (the film roughness is large, of rms = 8.3 nm). The roughness changes the length of oxygen vacancy migration paths and may also enhance locally the electric field, contributing to preferred nucleation

sites. Regarding the effect of the polymorph composition, the filament is expected to be more likely to form with an increasing amount of o-ErMnO₃, which is indeed observed. There is a remarkable decrease in V_{Form} (from ~ -9.5 V for 2% o-ErMnO₃ down to ~ -5.8 V for 50% o-ErMnO₃) and, importantly, in the variability of V_{Set} with an IQR from 3.3 V for 2% down to ~ 1.3 V for 50% o-ErMnO₃ (Fig. 4h). A higher o-ErMnO₃ content means overall more oxygen vacancies and more phase boundaries between the hexagonal and orthorhombic phases. Hence, the decrease of V_{Set} and of its variability with increasing amount of o-ErMnO₃ indicate that the formation of the conductive filament is likely to happen within the orthorhombic phase or at the boundary between the two phases. A previous study on YMnO₃ suggested that the boundaries between orthorhombic and hexagonal phases are oxygen-deficient regions¹⁹.

In conclusion, an increased fraction of the orthorhombic phase allows for reducing the operating voltage ($V_{\text{Form}} \sim -5.8$ V, $V_{\text{Set}} \sim -2.1$ V for 50% o-ErMnO₃) and the V_{Set} variability while keeping a large $R_{\text{OFF}}/R_{\text{ON}}$ of 10^4 . An adequate mixture of o-ErMnO₃ and h-ErMnO₃ polycrystalline phases provides a route to design low-voltage operating memristive devices as compared to reported devices based on hexagonal RMnO₃ films.

Let us now discuss the specificities of the switching mechanism involved in these polymorph ErMnO₃ devices compared to other existing metal oxide ones. Here, the mixed-phase structure of ErMnO₃ plays a critical role in optimizing the resistive switching behavior. On the one hand, the orthorhombic phase (and/or its boundary with the hexagonal phase) provides a reservoir of oxygen vacancies and provides pathways for their migration, enabling the filament formation/growth and therefore the switching behavior. On the other hand, the hexagonal phase avoids excessive leakage currents in the devices and stabilizes the switching process. The balance between these phases is crucial: too much orthorhombic phase ($\geq \sim 60\%$) leads to excessive leakage currents and no switching, while too much hexagonal phase limits the availability of oxygen vacancies (primarily in the orthorhombic phase or at the boundaries between the two polymorphs), leading, in particular, to large V_{Set} and V_{Sel} variability values.

This switching mechanism based on the coexistence of the two polymorphs is different from other materials where a phase transition, with the possible co-existence of the two crystalline phases, is the triggering factor for the resistive switching. In VO₂, the resistive switching is driven by the Mott transition between the insulating monoclinic phase and the metallic rutile phase⁶³. In TaO₂, the resistive switching is driven by the metal-insulator transition between the metallic rutile phase and the insulating triclinic phase⁶⁴. In manganite oxides like La_{2/3}Sr_{1/3}O₃ the movement of oxygen vacancies induce a phase transition (from the Perovskite phase to the Brownmillerite one)⁶⁵. The resistive switching in the above example originates from the change in crystalline phase and not, like in ErMnO₃ polymorph films, on the coexistence of two phases, that each bring its contribution to the resistive switching properties. In the study of Edwards et al. on BiFeO₃ devices, the introduction of the rhombohedral phase led to high rhombohedral-tetragonal boundary densities, resulting in increased current flow, while its removal under electric field application eliminated these conductive interfaces, resulting in large ON/OFF ratios between the two states⁶⁶. In our devices, the phase boundaries between orthorhombic and hexagonal phases also play a crucial role in defining the switching properties. However, in our case, oxygen vacancy migration at these phase boundaries and filament formation, rather than phase transition-driven conductivity changes, is the primary mechanism for resistive switching.

The switching in our devices also differs strongly from previously reported studies on RMnO₃-based devices (mainly h-YMnO₃)^{13–18}. A recent comparison of the different stacks and mechanisms is given in ref. 19. Unipolar resistive switching has been reported with polycrystalline hexagonal-YMnO₃ devices, where the mechanism was filamentary—either with Mn vacancies¹³ or oxygen vacancies¹⁴. It was suggested that the oxygen vacancy filaments formed/propagated along grain boundaries and charged domain walls. Bipolar resistive switching with polycrystalline h-YMnO₃ was also observed¹⁶. In addition, interface engineering and cation doping have been employed to further tailor switching behavior in h-YMnO₃, enabling

electroforming-free operation or inducing interface-type bipolar switching by modifying the barrier at the electrode interface^{15,17,18}.

In our mixed-phase ErMnO_3 films, the switching path is located at the boundaries between orthorhombic and hexagonal phases or within the orthorhombic phase (not in the hexagonal one). Note that the existence of charged domain walls is unlikely in our case. A study has indeed shown that the ferroelectric domain size in ErMnO_3 ceramics increases with decreasing grain size¹². For a grain size of $1.5\ \mu\text{m}$ and below, the ceramics exhibit a single domain configuration for the polarization. Since the grain size in our films is of $\sim 50\ \text{nm}$ (from the SEM images), the films exhibit most likely a monopolar configuration, hence without polar domain walls.

Note that none of the previous studies on polycrystalline RMnO_3 devices addresses the possible coexistence of hexagonal and orthorhombic phases. The minor presence of an orthorhombic phase cannot be ascertained from X-ray diffraction. We believe that it is unlikely that YMnO_3 polycrystalline films grown on a metallic substrate can be purely hexagonal due to the ease of formation of the metastable phase formation under stress/strain, which occurs upon cooling down whenever films are grown or annealed at a high temperature (the Gibbs energy difference is smaller than $5\ \text{kJ/mol}$ between o- and h- YMnO_3 ³³).

In our work, each polymorph brings in a specific role. Increasing the amount of the orthorhombic phase while keeping leakage currents low enough to not supersede resistive switching—thanks to the hexagonal phase—allows to significantly lower the Set voltage down to about $2\ \text{V}$ and to lower the variability inherent to filament formation.

Conclusion

Bipolar resistive switching behavior was demonstrated in polycrystalline mixed hexagonal/orthorhombic ErMnO_3 -based devices. The presence of the metastable orthorhombic phase was evidenced through a set of correlative microscopies (optical microscopy, SEM, c-AFM) and Raman spectroscopy. A straightforward method using optical microscopy or SEM was developed to quantify the fraction of the two crystalline phases. The operating voltage V_{Set} of the devices and its variability can be strongly decreased by increasing the amount of orthorhombic phase, with a 50% orthorhombic fraction showing the best performance. Devices with higher orthorhombic content ($>60\%$) exhibited increased leakage currents and failed to switch, indicating the critical role of the hexagonal phase in maintaining device functionality. The underlying mechanism of the resistive switching in these devices is attributed to the formation and rupture of conductive filament(s) based on oxygen vacancies, which likely occurs either in the orthorhombic phase or at the boundary between the two polymorphs. This hypothesis would need further validation through additional experiments, such as atom probe tomography or operando scanning transmission electron microscopy. This work provides key insights into the respective role of the polymorphs in ErMnO_3 -based devices and provides an engineering route for optimizing such devices.

Methods

ErMnO_3 film preparation and device fabrication

A Pt bottom electrode ($200\ \text{nm}$) with an adhesion layer of Ti ($30\ \text{nm}$) was deposited by electron-beam evaporation on $1\ \mu\text{m}$ -thick SiO_2/Si substrates. Pre-defined ErMnO_3 areas of $100 \times 100\ \mu\text{m}^2$ on the $\text{Si}/\text{SiO}_2/\text{Ti}/\text{Pt}$ substrates were patterned using photolithography with AZ5214E photoresist (Fig. 1a(i)). ErMnO_3 was deposited amorphous by Radio Frequency (RF) sputtering (Van Ardenne tool) at room temperature in an Ar ambient environment, with a RF power of $200\ \text{W}$ and an Ar pressure of $10\ \mu\text{bar}$ (Fig. 1a(ii)). The thickness of ErMnO_3 was measured by spectroscopic ellipsometry to be $60 \pm 1\ \text{nm}$. A lift-off process was used to remove the resist, leaving the patterned ErMnO_3 areas. It was followed by a post-deposition annealing step at $750\ ^\circ\text{C}$ for $30\ \text{min}$ in a furnace under N_2 atmosphere, resulting in polycrystalline ErMnO_3 (Fig. 1a(iii)). To pattern the top metal contact, another photoresist layer (AZ5214E) was spin-coated on the annealed ErMnO_3 film and exposed using photolithography (Fig. 1a(iv)). A top electrode of Ti ($20\ \text{nm}$) with a capping layer of Au ($50\ \text{nm}$) was

deposited by thermal evaporation, and another top electrode of Pt ($50\ \text{nm}$) was deposited by electron-beam evaporation, respectively (Fig. 1a(v)). Finally, fabricated Pt/ $\text{ErMnO}_3/\text{Ti}/\text{Au}$ and Pt/ ErMnO_3/Pt stacks, with device dimensions of $95 \times 95\ \mu\text{m}^2$, were obtained after the lift-off process (Fig. 1a(vi)).

Structural and microstructural characterization

Grazing incidence X-ray diffraction was performed to identify the crystalline structures of ErMnO_3 . A Panalytical MPD diffractometer was used. The incident angle was $\omega = 1^\circ$ and the wavelength was Cu K α ($1.54\ \text{\AA}$). The surface morphology of ErMnO_3 structures was characterized by optical microscopy (MPI AMZ12 microscope) and scanning electron microscopy (ZEISS-Gemini) at $10.0\ \text{kV}$ acceleration voltage. Scanning confocal Raman spectroscopy (Horiba LabRam) was performed with a $325\ \text{nm}$ laser in backscatter configuration to study the different crystalline phases.

Electrical characterization

Current-voltage ($I-V$) measurements were performed on Pt/ $\text{ErMnO}_3/\text{Ti}/\text{Au}$ and Pt/ ErMnO_3/Pt stacks using a semiconductor analyzer Keysight B1500 and a MPI TS2000-SE electrical probe station. During the measurements, the Pt bottom electrode was grounded, and a DC bias was applied to the top electrodes. The sweep rates were $75\ \text{mV/s}$ for negative bias and $15\ \text{mV/s}$ for positive bias. c-AFM was conducted using a Park Systems NX10 microscope to spatially map the local conductance of the films. During the measurements, the AFM probe tip (HQ:NSC14/Pt) was grounded and a DC bias was applied to the Pt bottom electrode.

Data availability

The data that support the findings of this study are available from the corresponding author upon reasonable request.

Received: 28 December 2024; Accepted: 24 August 2025;

Published online: 12 September 2025

References

1. Fiebig, M. et al. Determination of the magnetic symmetry of hexagonal manganites by second harmonic generation. *Phys. Rev. Lett.* **84**, 5620–5623 (2000).
2. Choi, T. et al. Insulating interlocked ferroelectric and structural antiphase domain walls in multiferroic YMnO_3 . *Nat. Mater.* **9**, 253–258 (2010).
3. Jungk, T., Hoffmann, Á, Fiebig, M. & Soergel, E. Electrostatic topology of ferroelectric domains in YMnO_3 . *Appl. Phys. Lett.* **97**, 012904 (2010).
4. Schultheiß, J. et al. Intrinsic and extrinsic conduction contributions at nominally neutral domain walls in hexagonal manganites. *Appl. Phys. Lett.* **116**, 262903 (2020).
5. Turner, P. W. et al. Large carrier mobilities in ErMnO_3 conducting domain walls revealed by quantitative Hall-effect measurements. *Nano Lett.* **18**, 6381–6386 (2018).
6. Schaab, J. et al. Electrical half-wave rectification at ferroelectric domain walls. *Nat. Nanotechnol.* **13**, 1028–1034 (2018).
7. Mosberg, A. B. et al. FIB lift-out of conducting ferroelectric domain walls in hexagonal manganites. *Appl. Phys. Lett.* **115**, 1–5 (2019).
8. Meier, D. et al. Anisotropic conductance at improper ferroelectric domain walls. *Nat. Mater.* **11**, 284–288 (2012).
9. Schultheiß, J. et al. Charged ferroelectric domain walls for deterministic ac signal control at the nanoscale. *Nano Lett.* **21**, 9560–9566 (2021).
10. Ruff, A. et al. Frequency-dependent polarisation switching in h- ErMnO_3 . *Appl. Phys. Lett.* **112**, 182908 (2018).
11. McCartan, J. et al. Fundamental aspects of conduction in charged ErMnO_3 domain walls. *Adv. Electron. Mater.* **2400091** <https://doi.org/10.1002/aelm.202400091> (2024).
12. Schultheiß, J. et al. Confinement-driven inverse domain scaling in polycrystalline ErMnO_3 . *Adv. Mater.* **34**, 2203449 (2022).

13. Yan, Z. B., Li, S. Z., Wang, K. F. & Liu, J. M. Unipolar resistive switching effect in $\text{YMn}_{1-\delta}\text{O}_3$ thin films. *Appl. Phys. Lett.* **96**, 012103 (2010).
14. Bogusz, A. et al. Resistive switching in polycrystalline YMnO_3 thin films. *AIP Adv.* **4**, 107135 (2014).
15. Rayapati, V. R. et al. Electroforming-free resistive switching in polycrystalline YMnO_3 thin films. *J. Appl. Phys.* **124**, 144102 (2018).
16. Wei, L., Jia, C. H. & Zhang, W. F. Distinguish and control the multi-level resistive switching for ferroelectric layer and interface in a $\text{YMnO}_3/\text{Nb}: \text{SrTiO}_3$ device. *RSC Adv.* **6**, 1445–1451 (2016).
17. Rayapati, V. R. et al. Electroforming-free resistive switching in yttrium manganite thin films by cationic substitution. *J. Appl. Phys.* **126**, 074102 (2019).
18. Rathod, K. N. et al. Extraction of switching parameters for Sr-doped YMnO_3 thin film. *Phys. Status Solidi ((A)) Appl. Mater. Sci.* **216**, 1–5 (2019).
19. Wu, R. et al. Electrochemical metallization memristive devices with Al active electrode using engineered mixed hexagonal/orthorhombic polycrystalline YMnO_3 . *Small Struct.* **5**, 2300494 (2024).
20. Bosak, A. A., Dubourdieu, C., Sénaire, J. P., Gorbenko, O. Y. & Kaul, A. R. Hexagonal rare earth (R=Eu-Dy) manganites: XRD study of epitaxially stabilized films. *Cryst. Eng.* **5**, 355–364 (2002).
21. Graboy, I. E. et al. HREM study of epitaxially stabilized hexagonal rare earth manganites. *Chem. Mater.* **15**, 2632–2637 (2003).
22. Ishiwata, S., Tokunaga, Y., Taguchi, Y. & Tokura, Y. High-pressure hydrothermal crystal growth and multiferroic properties of a perovskite YMnO_3 . *J. Am. Chem. Soc.* **133**, 13818–13820 (2011).
23. Počuča-Nešić, M. et al. Mechanochemical synthesis of yttrium manganite. *J. Alloy. Compd.* **552**, 451–456 (2013).
24. Waintal, A. & Chenavas, J. Transformation sous haute pression de la forme hexagonale de $\text{MnT}'\text{O}_3$ ($T' = \text{Ho}, \text{Er}, \text{Tm}, \text{Yb}, \text{Lu}$) en une forme perovskite. *Mater. Res. Bull.* **2**, 819–822 (1967).
25. Uusi-Esko, K., Malm, J., Imamura, N., Yamauchi, H. & Karppinen, M. Characterization of RMnO_3 ($R = \text{Sc}, \text{Y}, \text{Dy-Lu}$): High-pressure synthesized metastable perovskites and their hexagonal precursor phases. *Mater. Chem. Phys.* **112**, 1029–1034 (2008).
26. Lin, C. et al. Phase transformation in hexagonal ErMnO_3 under high pressure. *J. Appl. Phys.* **112**, 113512 (2012).
27. Kawazoe, Y., Kanomata, T. & Note, R. o-HoMnO₃ (Synthesized under pressure). in *High Pressure Materials Properties: Magnetic Properties of Oxides Under Pressure* 661–663 (Springer, 2023).
28. Salvador, P. A., Doan, T. D., Mercey, B. & Raveau, B. Stabilization of YMnO_3 in a perovskite structure as a thin film. *Chem. Mater.* **10**, 2592–2595 (1998).
29. Bosak, A. A. et al. Epitaxial phase stabilization phenomena in rare-earth manganites. *Thin Solid Films* **400**, 149–153 (2001).
30. Wunderlich, R. et al. Structural, magnetic and electric properties of HoMnO₃ films on SrTiO₃(001). *J. Magn. Magn. Mater.* **324**, 460–465 (2012).
31. Windsor, Y. W. et al. Multiferroic properties of o-LuMnO₃ controlled by b-axis strain. *Phys. Rev. Lett.* **113**, 167202 (2014).
32. Bosak, A. A., Dubourdieu, C., Sénaire, J. P., Gorbenko, O. Y. & Kaul, A. R. Epitaxial stabilization of hexagonal RMnO_3 ($R = \text{Eu-Dy}$) manganites. *J. Mater. Chem.* **12**, 800–801 (2002).
33. Yakel, H. L. et al. On the crystal structure of the manganese(III) trioxides of the heavy lanthanides and yttrium. *Acta Cryst.* **16**, 957–962 (1963).
34. Sánchez-Pérez, M. et al. Influence of the orthorhombic phase content on the dielectric and magnetic properties of YMnO_3 . *J. Appl. Phys.* **126**, 224103 (2019).
35. Gebhardt, E. & Köster, W. Das System Platin-Kobalt mit besonderer Berücksichtigung der Phase CoPt. *Int. J. Mater. Res.* **32**, 253–261 (1940).
36. Ye, F. et al. Incommensurate magnetic structure in the orthorhombic perovskite ErMnO_3 . *Phys. Rev. B Condens. Matter Mater. Phys.* **76**, 060402 (2007).
37. Hunnestad, K. A., Roede, E. D., Van Helvoort, A. T. J. J. & Meier, D. Characterization of ferroelectric domain walls by scanning electron microscopy. *J. Appl. Phys.* **128**, 191102 (2020).
38. Roede, E. D. et al. Contact-free reversible switching of improper ferroelectric domains by electron and ion irradiation. *APL Mater.* **9**, 021105 (2021).
39. Chen, Y. et al. Domain structure and multiferroic properties of epitaxial hexagonal ErMnO_3 films. *J. Alloy. Compd.* **821**, 3–8 (2020).
40. Vermette, J., Jandl, S. & Gospodinov, M. M. Raman study of spin–phonon coupling in ErMnO_3 . *J. Phys. Condens. Matter* **20**, 425219 (2008).
41. Skjærø, S. H. et al. Interstitial oxygen as a source of p-type conductivity in hexagonal manganites. *Nat. Commun.* **7**, 13745–13745 (2016).
42. Massa, N. E. et al. Far- and mid-infrared emission and reflectivity of orthorhombic and cubic ErMnO_3 : polarons and bipolarons. *Phys. Rev. B* **98**, 184302 (2018).
43. Liu, C. Y., Ho, J. Y., Huang, J. J. & Wang, H. Y. Transient current of resistive switching of a NiOx resistive memory. *Jpn. J. Appl. Phys.* **51**, 041101 (2012).
44. Kuo, H. Y., Cheng, Y. H., Chang, H., Shaw, J. S. & Lee, R. Design of electrodes on gold test strips for enhanced accuracy in glucose measurement. *J. Sens.* **2019**, 1–10 (2019).
45. Sassine, G. et al. Interfacial versus filamentary resistive switching in TiO_2 and HfO_2 devices. *J. Vac. Sci. Technol. B* **34**, 012202 (2016).
46. Chiu, F. C. Conduction mechanisms in resistance switching memory devices using transparent boron-doped zinc oxide films. *Materials* **7**, 7339–7348 (2014).
47. González-Flores, K. E. et al. Analysis of the conduction mechanisms responsible for multilevel bipolar resistive switching of SiO_2/Si multilayer structures. *Superlattices Microstruct.* **137**, 106347 (2020).
48. Waser, R., Dittmann, R., Staikov, C. & Szot, K. Redox-based resistive switching memories nanoionic mechanisms, prospects, and challenges. *Adv. Mater.* **21**, 2632–2663 (2009).
49. Dittmann, R., Menzel, S. & Waser, R. Nanoionic memristive phenomena in metal oxides: the valence change mechanism. *Adv. Phys.* **70**, 155–349 (2021).
50. Waser, R. & Aono, M. Nanoionics-based resistive switching memories. *Nanosci. Technol. A Collect. Rev. Nat. J.* **6**, 158–165 (2009).
51. Padovani, A., Larcher, L., Pavan, P., Cagli, C. & de Salvo CEA, B. Understanding the role of the Ti metal electrode on the forming of HfO_2 -based RRAMs. In *Proc. 4th International Memory Workshop 1–4* (Milan, Italy, 2012). <https://doi.org/10.1109/IMW.2012.6213667> (IEEE, 2012).
52. Tsai, Y. T. et al. Effect of top electrode material on resistive switching characteristics in MnO_2 nonvolatile memory devices. *ECS Trans.* **41**, 475–482 (2011).
53. Lin, C. Y. et al. Effect of top electrode material on resistive switching properties of ZrO_2 film memory devices. *IEEE Electron Device Lett.* **28**, 366–368 (2007).
54. Nagashima, K., Yanagida, T., Oka, K. & Kawai, T. Unipolar resistive switching characteristics of room temperature grown SnO_2 thin films. *Appl. Phys. Lett.* **94**, 242902 (2009).
55. Sharma, Y., Misra, P., Pavunny, S. P. & Katiyar, R. S. Multilevel unipolar resistive memory switching in amorphous SmGdO_3 thin film. *Appl. Phys. Lett.* **104**, 073501 (2014).
56. Sharma, Y., Misra, P., Pavunny, S. P. & Katiyar, R. S. Unipolar resistive switching behavior of high-k ternary rare-earth oxide LaHoO_3 thin films for non-volatile memory applications. *Mater. Res. Soc. Symp. Proc.* **1729**, 23–28 (2015).
57. Chiu, F.-C. A review on conduction mechanisms in dielectric films. *Adv. Mater. Sci. Eng.* **2014**, 578168 (2014).
58. Sze, S. M. & Ng, K. K. *Physics of Semiconductor Devices* (John Wiley & Sons, Inc., 2006).

59. Kalashnikova, A. M. & Pisarev, R. V. Electronic structure of hexagonal rare-earth manganites RMnO_3 . *J. Exp. Theor. Phys. Lett.* **78**, 143–147 (2003).
60. Ren, C.-Y. Atomic, electronic, and ferroelectric properties of manganite RMnO_3 ($\text{R} = \text{Ho}, \text{Er}, \text{Tm}, \text{Lu}$) in hexagonal and orthorhombic phases. *Phys. Rev. B* **79**, 125113 (2009).
61. Alonso, J. A., Martínez-Lope, M. J., Casais, M. T. & Fernández-Díaz, M. T. Evolution of the Jahn-Teller distortion of MnO_6 octahedra in RMnO_3 perovskites ($\text{R} = \text{Pr}, \text{Nd}, \text{Dy}, \text{Tb}, \text{Ho}, \text{Er}, \text{Y}$): a neutron diffraction study. *Inorg. Chem.* **39**, 917–923 (2000).
62. Todd, P. K. et al. Defect-accommodating intermediates yield selective low-temperature synthesis of YMnO_3 polymorphs. *Inorg. Chem.* **59**, 13639–13650 (2020).
63. Lee, W. et al. Vanadium oxide thin film deposited on Si by atomic layer deposition for non-volatile resistive switching memory devices. *Appl. Surf. Sci.* **639**, 158240 (2023).
64. Zhu, L., Zhou, J., Guo, Z. & Sun, Z. Realization of a reversible switching in TaO_2 polymorphs via Peierls distortion for resistance random access memory. *Appl. Phys. Lett.* **106**, 091903 (2015).
65. Yao, L., Inkinen, S. & Van Dijken, S. Direct observation of oxygen vacancy-driven structural and resistive phase transitions in $\text{La}_{2/3}\text{Sr}_{1/3}\text{MnO}_3$. *Nat. Commun.* **8**, 14544 (2017).
66. Edwards, D. et al. Giant resistive switching in mixed-phase BiFeO_3 : via phase population control. *Nanoscale* **10**, 17629–17637 (2018).
67. Wu, R. Resistive Switching in Mixed Orthorhombic/hexagonal RMnO_3 ($\text{R} = \text{Y}, \text{Er}$) Polycrystalline Thin Films. Doctoral Thesis (Freie Universität Berlin, 2024).
68. Martín-Carrón, L., De Andrés, A., Martínez-Lope, M. J., Casais, M. T. & Alonso, J. A. Raman phonons as a probe of disorder, fluctuations, and local structure in doped and undoped orthorhombic and rhombohedral manganites. *Phys. Rev. B* **66**, 174303 (2002).
69. Iliev, M. N. et al. Raman active phonons in orthorhombic YMnO_3 and LaMnO_3 . *J. Phys. Chem. Solids* **59**, 1982–1984 (1998).
70. Iliev, M. & Abrashev, M. Raman spectroscopy of orthorhombic perovskitelike YMnO_3 and LaMnO_3 . *Phys. Rev. B Condens. Matter Mater. Phys.* **57**, 2872–2877 (1998).

Acknowledgements

The text and results of this article are part of the doctoral thesis of Dr. Rong Wu⁶⁷. The authors acknowledge funding by the BMBF in the framework of the ForMikro project ERMI (Erforschung rekonfigurierbarer, passiver Mikroelektronikbauelemente für Energieeffizienz und Flexibilität). The authors acknowledge the cooperation and funding of Park Systems for the study by AFM and c-AFM. The authors acknowledge the Center for Correlated Microscopy and Spectroscopy at HZB and the support from Dr. Luca Sulmoni and Stefan Bock at the clean room of the Technische Universität Berlin. The authors are grateful for the technical support from Jürgen Albert and Sven Wiesner.

Author contributions

C.D. initiated and coordinated the study. R.W. grew and characterized the ErMnO_3 thin films, fabricated the devices and performed the electrical measurements with contributions from C.D., V.D., F.M., T.L.P., and S.W.S. All authors discussed the results. The manuscript was written by R.W., C.D., F.M., and T.L.P. All co-authors edited the manuscript.

Funding

Open Access funding enabled and organized by Projekt DEAL.

Competing interests

The authors declare no competing interests.

Additional information

Supplementary information The online version contains supplementary material available at <https://doi.org/10.1038/s43246-025-00929-6>.

Correspondence and requests for materials should be addressed to Rong Wu or Catherine Dubourdieu.

Peer review information *Communications Materials* thanks Muhammad Naqi and Heekyeong Park for their contribution to the peer review of this work. Primary handling editors: Sunkook Kim and Aldo Isidori. A peer review file is available.

Reprints and permissions information is available at <http://www.nature.com/reprints>

Publisher's note Springer Nature remains neutral with regard to jurisdictional claims in published maps and institutional affiliations.

Open Access This article is licensed under a Creative Commons Attribution 4.0 International License, which permits use, sharing, adaptation, distribution and reproduction in any medium or format, as long as you give appropriate credit to the original author(s) and the source, provide a link to the Creative Commons licence, and indicate if changes were made. The images or other third party material in this article are included in the article's Creative Commons licence, unless indicated otherwise in a credit line to the material. If material is not included in the article's Creative Commons licence and your intended use is not permitted by statutory regulation or exceeds the permitted use, you will need to obtain permission directly from the copyright holder. To view a copy of this licence, visit <http://creativecommons.org/licenses/by/4.0/>.

© The Author(s) 2025